THE JOURNAL OF PHYSICAL CHEMISTRY C
A JOURNAL OF THE AMERICAN CHEMICAL SOCIETY

pubs.acs.org/JPCC

Article

Tunable Ti^{3+}-Mediated Charge Carrier Dynamics of Atomic Layer Deposition-Grown Amorphous TiO_2

Jesse Saari, Harri Ali-Löytty,* Minttu Maria Kauppinen, Markku Hannula, Ramsha Khan, Kimmo Lahtonen, Lauri Palmolahti, Antti Tukiainen, Henrik Grönbeck, Nikolai V. Tkachenko, and Mika Valden*

Cite This: *J. Phys. Chem. C* 2022, 126, 4542−4554

Read Online

ACCESS | Metrics & More | Article Recommendations | Supporting Information

ABSTRACT: Amorphous titania (am.-TiO_2) has gained wide interest in the field of photocatalysis, thanks to exceptional disorder-mediated optical and electrical properties compared to crystalline TiO_2. Here, we study the effects of intrinsic Ti^{3+} and nitrogen defects in am.-TiO_2 thin films via the atomic layer deposition (ALD) chemistry of tetrakis(dimethylamido)titanium-(IV) (TDMAT) and H_2O precursors at growth temperatures of 100−200 °C. X-ray photoelectron spectroscopy (XPS) and computational analysis allow us to identify structural disorder-induced penta- and heptacoordinated Ti^{4+} ions ($Ti_{5/7c}^{4+}$), which are related to the formation of Ti^{3+} defects in am.-TiO_2. The Ti^{3+}-rich ALD-grown am.-TiO_2 has stoichiometric composition, which is explained by the formation of interstitial peroxo species with oxygen vacancies. The occupation of Ti^{3+} 3d in-gap states increases with the ALD growth temperature, inducing both visible-light absorption and electrical conductivity via the polaron hopping mechanism. At 200 °C, the in-gap states become fully occupied extending the lifetime of photoexcited charge carriers from the picosecond to the nanosecond time domain. Nitrogen traces from the TDMAT precursor had no effect on optical properties and only little on charge transfer properties. These results provide insights into the charge transfer properties of ALD-grown am.-TiO_2 that are essential to the performance of protective photoelectrode coatings in photoelectrochemical solar fuel reactors.

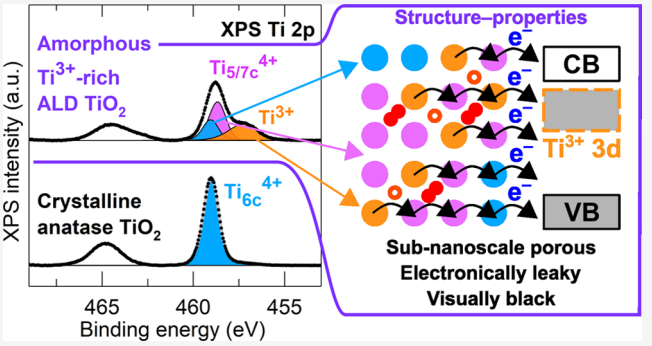

INTRODUCTION

Since the discovery of photoelectrochemical (PEC) water splitting introduced first by Fujishima and Honda in 1972 using n-type rutile titanium dioxide (TiO_2), photocatalysts based on crystalline TiO_2 have been widely studied materials.[1] Doping crystalline TiO_2 with substitutional nitrogen is an efficient means to extend the light absorption from UV to visible range and enable visible-light active TiO_2.[2] Recently, immense interest in amorphous TiO_2 (am.-TiO_2) has emerged for its exceptional charge transfer properties in photocatalytic applications. Based on computational studies, the am.-TiO_2 structure consists of mainly Ti−O_6 octahedra and also under- (e.g., Ti_{5c}) and overcoordinated (e.g., Ti_{7c}) titanium ions, whereas in crystalline TiO_2 only six-coordinated (Ti_{6c}) ions are present.[3,4] For example, in computational models of am.-TiO_2, pentacoordinated Ti ions (Ti_{5c}) are reported to be rather abundant (>20%).[3,5] However, experimental methods for the analysis of the amorphous structure considering coordination numbers of Ti ions are rarely reported. The disordered structure of am.-TiO_2 can induce exceptional optical and electrical properties that have been demonstrated to improve photocatalytic activity and protect photoelectrodes in photoelectrochemical cells.[6−8] Particularly, amorphous "black" titania is regarded as a significant potential material for photocatalytic applications.[7,9,10]

Atomic layer deposition (ALD) is known for providing thin films with excellent controllability, uniformity, and conformality, and provides a potential method to modify the TiO_2 defect composition in a controlled manner via surface chemical reactions.[11−14] Particularly, the ALD growth temperature is an essential factor affecting surface reaction pathways during the growth process.[15,16] For example, an alkylamido organometallic ALD precursor, tetrakis(dimethylamido)titanium (TDMAT), has been shown to leave nitrogen residues into as-grown TiO_2 thin films, especially at lower growth temperatures.[13,17,18] Use of a higher growth temperature (200 °C) has been found to decrease the amount of nitrogen but

Received: December 29, 2021
Revised: February 15, 2022
Published: February 25, 2022

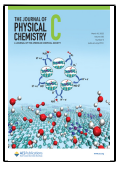

simultaneously result in the formation of Ti^{3+} species.[12,13,19] These Ti^{3+} defects can increase electrical conductivity and induce visible-light absorption in am.-TiO_2.[12] The mechanism is different from the visible absorption induced by substitutional nitrogen doping of crystalline TiO_2 but similar to the hydrogenated "black" TiO_2 that can be also categorized as reduced TiO_2 with a disordered structure.[7,12,19−22] The commonly accepted view is that an oxygen vacancy within TiO_2 is surrounded by three pentacoordinated Ti_{5c} ions and initially two of them are Ti^{3+} ions.[20,23] These Ti^{3+} defects carry unpaired excess electrons that can couple with phonons from vibrations of surrounding ions and form quasiparticles called electron polarons.[7,24] These polarons can hop from Ti^{3+} ion to an adjacent Ti^{4+} ion converting it to a Ti^{3+} ion, which is known as polaron hopping[24,25] Based on molecular dynamics simulations, Deskins et al. proposed that electron transport in amorphous TiO_2 depends on the distances between adjacent Ti^{4+} ions, whereas hole transport is related to the distances between Ti^{3+} ions.[4] Consequently, these computational results imply that the polaron hopping mechanism is responsible for the conductivity of TiO_2 and strongly related to the concentration of Ti^{3+} defects.[4,7,20,25] This charge transport mechanism and its relation to the Ti^{3+} defects is also supported by experimental studies.[21,26] Furthermore, Ti^{3+} defects form energy states within the band gap enabling light absorption in the visible range.[7,12,27,28]

Regarding charge carrier dynamics and kinetics, careful investigation of in-gap states, especially electron and hole traps, in am.-TiO_2 is needed.[28] According to the current understanding, the disordered structure, undercoordinated ions, and elongated metal−oxygen bonds in amorphous metal oxides may induce electron and hole traps in the band gap.[5,29] Additionally, Ti^{3+} defects have been reported to generate in-gap trap states with intrinsic self-trapped electrons.[20,28,30] However, the nature and relationship of these trap states and the structure of am.-TiO_2 are still under debate. Experimentally, in-gap trap states have been studied by various methods, such as photoelectron spectroscopy (PES) and transient absorption spectroscopy (TAS).[28,31−33] Based on the reported PES valence band (VB) spectra, electron trap states of TiO_2 are commonly located around 0.2−1.2 eV below the Fermi level.[21,24,26,28,31] Transient absorption spectroscopy, instead, provides a method to study the dynamics of charge carriers, and thus determine, e.g., carrier lifetime that is a critical factor to determine the photocatalytic activity of a material.[32−35]

This work utilizes X-ray photoelectron spectroscopy (XPS) analysis and density functional theory (DFT) calculations to identify structural disorder-induced penta- and heptacoordinated Ti ions ($Ti_{5/7c}^{4+}$), and examines how titanium and nitrogen defects of amorphous TiO_2 can be controlled by the ALD growth temperature while using TDMAT and H_2O as precursors. The lower deposition temperature causes trapping and adsorption of nitrogen-containing reaction byproducts, whereas the higher growth temperature leads to enhanced byproduct desorption as well as increased concentration of Ti^{3+} and penta-/heptacoordinated $Ti_{5/7c}^{4+}$ species. The structural disorder of am.-TiO_2 involving under- and overcoordinated Ti ions is found to provide trap states for charge carriers, which recombine in the picosecond time domain. Ti^{3+} defects with intrinsic self-trapped electrons in the band gap states allow visible-light absorption, extend charge carrier lifetime to the nanosecond (ns) time domain, and induce electrical conductivity. The structural disorder alone induces only broadening of core-level peaks, whereas the formation of Ti^{3+} defects mediates a chemical shift also in the 2p binding energy of neighboring Ti^{4+} ions. Controlling the optical and electrical properties of amorphous TiO_2 by modifying the defects is a promising approach to tailor optimized am.-TiO_2 thin films for many fields of applications including photocatalysis and protective photoelectrode coatings in photoelectrochemical solar fuel reactors.

EXPERIMENTAL SECTION

Substrates. The P-doped (resistivity: 1−10 Ω cm) n-Si(100) wafers from SIEGERT WAFER GmbH (Germany) cleaved into 10 mm × 10 mm × 0.525 mm pieces were used as substrates in photoelectron spectroscopy (PES), grazing incidence X-ray diffraction (GIXRD), and ellipsometry experiments. For UV−vis spectroscopy, transient absorption spectroscopy (TAS), and electrical conductivity measurements, UV-grade fused silica (quartz) (10 mm × 10 mm × 1 mm) from Präzisions Glas & Optik GmbH (Germany) was used as a substrate.

Atomic Layer Deposition. The ALD of TiO_2 was carried out using a Picosun Sunale ALD R-200 Advanced reactor and tetrakis(dimethylamido)titanium(IV) ($Ti(N(CH_3)_2)_4$, TDMAT, electronic grade 99.999+%, Sigma-Aldrich) and Milli-Q type 1 ultrapure water as precursors. To reach the proper TDMAT precursor vapor pressure, the bubbler was heated to 76 °C, and to prevent condensation of the precursor gas the delivery line was heated to 85 °C. The water bubbler was maintained at 18 °C using a Peltier element for stability control. Argon (99.9999%, Oy AGA Ab, Finland) was used as a carrier gas. During the deposition, the continuous Ar flow in the TDMAT and H_2O lines was 100 sccm. The ALD cycle consisted of the 1.6 s TDMAT pulse followed by the 0.1 s H_2O pulse. Between each pulse, the excess precursor was pumped during the 6.0 s purge period. TiO_2 films were deposited at the growth temperatures of 100, 150, 175, and 200 °C. The thicknesses of TiO_2 films were verified by ellipsometer (Rudolph Auto EL III Ellipsometer, Rudolph Research Analytical) using the helium−neon laser (λ = 632.8 nm) as a light source. The required number of ALD cycles for 30 nm thick TiO_2 at growth temperatures of 100, 150, 175, and 200 °C were 480, 636, 733, and 870, respectively. Based on the GIXRD measurements shown in Figure S1, the as-deposited 30 nm thick thin films grown at temperatures between 100 and 200 °C were amorphous.

Anatase TiO_2(30 nm) Reference. The anatase TiO_2(30 nm) samples were prepared from ALD TiO_2 (30 nm, 100 °C) grown on Si(100) substrates by a heat treatment in air at 500 °C for 45 min.

Photoelectron Spectroscopy (XPS, Ultraviolet Photoelectron Spectroscopy (UPS)). Photoelectron spectroscopy (PES) measurements consisting of X-ray photoelectron spectroscopy (XPS) and ultraviolet photoelectron spectroscopy (UPS) were conducted using a NanoESCA spectromicroscope (Omicron Nanotechnology GmbH) in ultra-high vacuum (UHV) with a base pressure below 1×10^{-10} mbar. For core-level XPS, focused monochromatized Al Kα ($h\nu$ = 1486.5 eV) was used as excitation radiation, whereas in UPS measurements focused non-monochromatized He Iα radiation ($h\nu$ = 21.22 eV) from HIS 13 VUV Source (Focus GmbH) was utilized to study the valence band structure. The angle-resolved XPS (ARXPS) measurements were carried out using non-monochromatized DAR400 X-ray source (Al Kα) and

https://doi.org/10.1021/acs.jpcc.1c10919
J. Phys. Chem. C 2022, 126, 4542−4554

Argus hemispherical electron spectrometer (Omicron Nanotechnology GmbH). The core-level XP spectra were analyzed by least-squares fitting of Gaussian−Lorentzian lineshapes and using a Shirley-type background. UPS valence band spectra were analyzed by fitting a Tougaard-type background. The Ti 2p spectra were fitted using the anatase TiO_2 Ti $2p_{3/2}$ reference peak shape for the six-coordinated Ti^{4+} peak (Ti_{6c}^{4+}), and the amorphous disordered structure was represented by the pentacoordinated Ti^{4+} (Ti_{5c}^{4+}) and Ti^{3+} peaks. The binding energy (BE) scale of the spectra was calibrated by fixing the O^{2-} peak of TiO_2 to 530.20 eV. CasaXPS version 2.3.22 PR1.0[36] was used as analysis software, and the Scofield photoionization cross-sections were used as relative sensitivity factors.[37]

Computational Analysis of Core-Level Shifts. Modeling the amorphous phase of titania (am.-TiO_2) is challenging due to its lack of long-range order and a defined crystal structure. Previous computational studies have employed molecular dynamics to generate structural models for am.-TiO_2 using the melt-and-quench method.[5,38] As the structural models for am.-TiO_2 necessarily have large unit cells containing >200 atoms, sampling the core-level shifts (CLSs) of all atoms for many structures becomes unfeasible. Moreover, it is not clear how representative the melt-and-quench structures are for the experimental am.-TiO_2 structures. Because of structural ambiguity, we performed calculations for both the crystalline anatase phase and a model of am.-TiO_2.

Spin-polarized calculations were performed using the Vienna Ab initio Simulation Package (VASP; version 5.4.4).[39−42] The GGA + U approach was employed using the Perdew−Burke−Ernzerhof (PBE) functional[43,44] with a Hubbard correction[45] of U = 4.2 eV applied to the 3d orbitals of Ti atoms. This value for the correction has been used previously in calculations involving amorphous TiO_2[38] and anatase;[46] see the Supporting Information for more details concerning the choice and impact of the U value. The valence−core interactions were treated with the projector augmented-wave (PAW) method,[47,48] and the valence configurations were $2s^22p^4$ (O) and $3s^23p^64s^23d^2$ (Ti). A plane-wave basis set with a cutoff energy of 500 eV was used for geometry optimizations and core-level shift calculations. The pristine anatase bulk was optimized using a 12 × 12 × 4 Γ-centered k-point mesh until residual forces were less than 0.01 eV/Å. The optimized lattice parameters are a = 3.86 and c = 9.74 Å, which are in fair agreement with experimental values (a = 3.78 Å, c = 9.51 Å).[49,50] The band gap was found to be 2.64 eV, which is close to the previously reported value of 2.87 eV using the PBE functional with a Hubbard-U value of 4.0 eV.[51] A 144 atom 4 × 3 × 1 supercell of the optimized bulk was used for subsequent calculations to reduce the interaction of the oxygen vacancy with its periodic image. Model structures for am-TiO_2 (15 in total) were obtained from the work of Mora-Fonz et al.[5] The unit cells and atomic positions of the model structures[5] were re-optimized using the present computational setups. The lowest energy structure (see Figure S2a) was used in the core-level shift calculations. Due to the large size of the amorphous TiO_2 unit cell and the large supercell for anatase, the sampling of the Brillouin zone was restricted to the Γ-point.

The oxygen vacancy formation energy E_f^{vac} was calculated as

$$E_f^{vac} = E_{tot}^{vac} + \frac{1}{2}E_{O_2} + E_{tot} \quad (1)$$

where E_{tot} is the total energy of the pristine structure, E_{tot}^{vac} is the total energy of the same structure containing a single oxygen vacancy, and E_{O_2} is the energy of an oxygen molecule in the gas phase. Bader charge analyses were performed using the code developed by the Henkelman group.[52−55]

CLSs were calculated with respect to a reference atom in the final state picture, i.e., complete screening of the core hole by valence electrons was assumed. The core-level shifts were computed systematically for all atoms in the supercells. The structures with a core hole in Ti 2p or O 1s were obtained using a PAW potential with an electron−hole in the 2p and 1s shell of Ti and O, respectively. As the studied systems have band gaps, the charge neutrality in the presence of a core hole was maintained by employing a homogeneous jellium background. To facilitate the comparison with experiments, a Gaussian fit was applied to the CLS peaks, with a standard deviation of 0.43. The parameters are chosen such that they reproduce a qualitatively similar width at half-maximum as the peaks in the experimental spectra. All CLS values were shifted so that the maximum of the largest fitted Gaussian peak was centered at zero.

Grazing Incidence X-ray Diffraction (GIXRD). The phase structure of the ALD TiO_2 samples was defined via grazing incidence X-ray diffraction (GIXRD, PANalytical X'Pert^3 MRD diffractometer) with Cu Kα radiation (λ = 1.5406 Å, $h\nu$ = 8.05 keV) and 45 kV and 40 mA cathode voltage and current, respectively. The samples were scanned in 2θ between 20 and 52° using grazing-incidence angle Ω = 0.3°. The background was removed from each of the scans to allow easier comparison of the measured GIXRD patterns.

Electrical Conductivity Measurement. Electrical conductivity was determined by measuring the sheet resistance of the am.-TiO_2 thin film grown on quartz substrates using the four-probe method. In the measurement, four nickel-plated tungsten probe tips (Picoprobe ST-20-5-NP, GGB Industries Inc.) were positioned on the sample surface (size 10 mm × 10 mm) in line with equal 2 mm spacing, and a linear scan voltammetry measurement was performed at 100 mV/s with an Autolab PGSTAT101 potentiostat (Metrohm AG). The sheet resistance, R_s, for the given configuration was calculated by

$$R_s = 0.7744 \cdot \frac{\pi}{\ln(2)} \frac{\Delta V}{I} \quad (2)$$

where ΔV is the voltage difference over the two inner probe tips, I is the current through the outer two probe tips, and the constant 0.7744 is the geometric correction factor.[56] Conductivity was then calculated as follows

$$\text{conductivity} = \frac{1}{\rho} = \frac{1}{R_s \cdot t} \quad (3)$$

where ρ is the film resistivity and t is the am.-TiO_2 film thickness.

Steady-State UV−Vis Spectroscopy. The optical properties were measured on 30 nm thick am.-TiO_2 films deposited on quartz substrates. Measurements were conducted by measuring both the transmission, T, and reflectance, R, of the am.-TiO_2 film with an integrating sphere module of a spectrophotometer (PerkinElmer 1050). A reflection-corrected formula was used for calculating the absorption $A = -\log[T/(1 - R)]$.[57]

https://doi.org/10.1021/acs.jpcc.1c10919
J. Phys. Chem. C 2022, 126, 4542−4554

Sub-Nanoscale Porosity Modeling. The sub-nanoscale porosity of ALD am.-TiO_2 thin films was determined based on the refractive index results measured by ellipsometer (Rudolph Auto EL III Ellipsometer, Rudolph Research Analytical) using the helium−neon laser (λ = 632.8 nm) as a light source and the Lorentz−Lorenz effective medium approximation (EMA).[58] The sub-nanoscale porosity was calculated using the EMA equation

$$\frac{n^2-1}{n^2+2} = (1-p)\frac{{n_{\text{anatase}}}^2-1}{{n_{\text{anatase}}}^2+2} + p\frac{{n_{\text{air}}}^2-1}{{n_{\text{air}}}^2+2} \quad (4)$$

where p is the sub-nanoscale porosity and n, n_{anatase}, and n_{air} are the refractive indices of am.-TiO_2, anatase TiO_2 reference (n = 2.396), and air (n = 1.000), respectively.

Transient Absorption Spectroscopy (TAS). Transient absorption spectra of all the samples were measured using a femtosecond pump−probe setup. The samples were excited with a wavelength of 320 nm in a transmittance mode in both UV−vis and near-infrared (NIR) regions. The fundamental laser pulses were generated using the Ti:sapphire laser, Libra F (Coherent Inc., 800 nm) with a repetition rate of 1 kHz. The fundamental beam was split into two, and the main part of the beam was directed onto the optical amplifier (Topas C, Light Conversion Ltd.) to produce the desired wavelength of 320 nm in our study. The rest of the fundamental beam was delivered to a white continuum generator (sapphire crystal) for sample probing. The probe light was further split into reference and signal beams, which were focused on the samples. The lifetime decay of the samples was measured up to 5 ns for all the samples.

RESULTS AND DISCUSSION

To investigate the effect of the ALD growth temperature on the chemical and electronic structures of am.-TiO_2, the 30 nm thick ALD am.-TiO_2 grown at 100, 150, 175, and 200 °C was measured by XPS and UPS. Figure 1 shows Ti 2p and O 1s XP spectra of the 30 nm thick ALD am.-TiO_2 deposited at different growth temperatures. Annealing the sample grown at 100 °C in air at 500 °C resulted in anatase TiO_2 (Figure S1), which served as a reference for the six-coordinated Ti^{4+} ($Ti_{6c}{}^{4+}$).[3,4] Anatase TiO_2 showed a narrow Ti $2p_{3/2}$ peak at 459.0 ± 0.1 eV that was fitted with a constrained peak width and position to the spectra recorded for ALD am.-TiO_2 samples. All of the Ti 2p spectra of ALD am.-TiO_2 thin films in Figure 1a show clear evidence of Ti^{3+} defects as a shoulder at 457.3 ± 0.1 eV.[12,19] The middle component is assigned to structural disorder-induced Ti^{4+} ions ($Ti_{5/6/7c}{}^{4+}$), which are related to the nearest or next-nearest neighbors of oxygen vacancies or interstitial peroxo species that are responsible for the formation of Ti^{3+} defects in am.-TiO_2. The peak separation in the binding energy (BE) between $Ti_{6c}{}^{4+}$ and $Ti_{5/6/7c}{}^{4+}$ peaks was 0.39 eV. Figure 1b shows that the O 1s peak consists mainly of the O−Ti component (O^{2-}) at 530.2 eV and a minor peak at 532.0 ± 0.2 eV, regardless of the ALD growth temperature. The component at higher BE is assigned to either −OH/O−C or interstitial peroxo ($O_2{}^{2-}$) species. Additionally, Figure S4 highlights the differences between Ti 2p spectra and the similarity of O 1s spectra shown in Figure 1. Interestingly, despite the distinct presence of oxygen vacancies-induced Ti^{3+} ions, the O/Ti atomic ratios of all am.-TiO_2 thin films are close to 2 (Figure S5), implying the displacement of oxygen ions within the films instead of removal of them upon vacancy formation. The result can be rationalized by the presence of local oxygen-rich centers such as interstitial peroxo species.

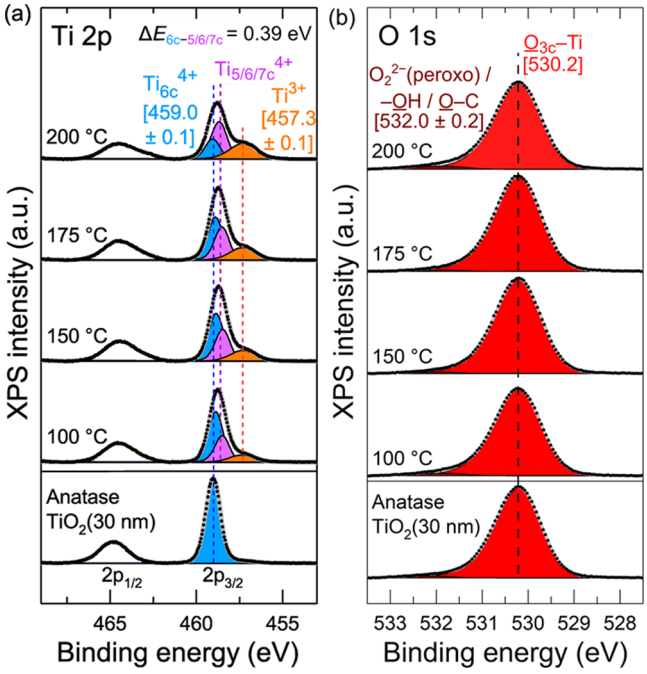

Figure 1. (a) Ti 2p and (b) O 1s XP spectra of the 30 nm thick ALD am.-TiO_2 grown at 100, 150, 175, and 200 °C. Anatase TiO_2 (30 nm) is used as a reference sample for the six-coordinated $Ti_{6c}{}^{4+}$ peak.

As a comparison with the proposed experimental XPS Ti 2p peak fitting (Figure 1), Figure S6 presents the more traditional peak fitting of the Ti^{4+} component and analysis of the full width at half-maximum (FWHM). The FWHM is clearly larger for am.-TiO_2 compared to crystalline anatase; moreover, the peak width increases as the ALD growth temperature is increased (details on the fitting parameters are presented in Table S2). The fitting results suggest that it is not sufficient to fit the Ti^{4+} 2p of am.-TiO_2 with only one component. Using a second component results in an adequate fit. A slight shift in the binding energy of $Ti_{6c}{}^{4+}$ and $Ti_{5/6/7c}{}^{4+}$ peak positions can originate from differences in the amount of more rare over- and undercoordinated Ti ions ($Ti_{8c}{}^{4+}$, $Ti_{7c}{}^{4+}$, $Ti_{4c}{}^{4+}$) and wide distributions of bond lengths and angles, which are also partly attributed to local effects of polarons.[3−5,24]

To the best of our knowledge, there are no previously reported efforts to identify Ti^{4+} ions ($Ti_{5/6/7c}{}^{4+}$), which are related to the nearest or next-nearest neighbors of oxygen vacancies, experimentally by photoelectron spectroscopy as proposed in this work. Therefore, we performed density functional theory calculations of CLSs mediated by an oxygen vacancy or interstitial peroxo species in anatase TiO_2 and an am.-TiO_2 structure. Figure 2 presents the results from the computational analysis of oxygen defect-induced CLSs in anatase TiO_2. In the case of pristine anatase, there were no CLSs in either Ti 2p or O 1s since all of the Ti/O sites have identical environments.

In the second case, the oxygen vacancy was formed by removing one of the lattice oxygens from the 144-atom bulk anatase supercell and re-relaxing the atomic positions of the resulting structure (see Figure 2c). Upon vacancy creation, the two excess electrons can either localize fully on nearby pentacoordinated Ti_{5c} cations or partially, with one electron on a Ti_{5c} ion and the other one delocalized over the entire

https://doi.org/10.1021/acs.jpcc.1c10919
J. Phys. Chem. C 2022, 126, 4542−4554

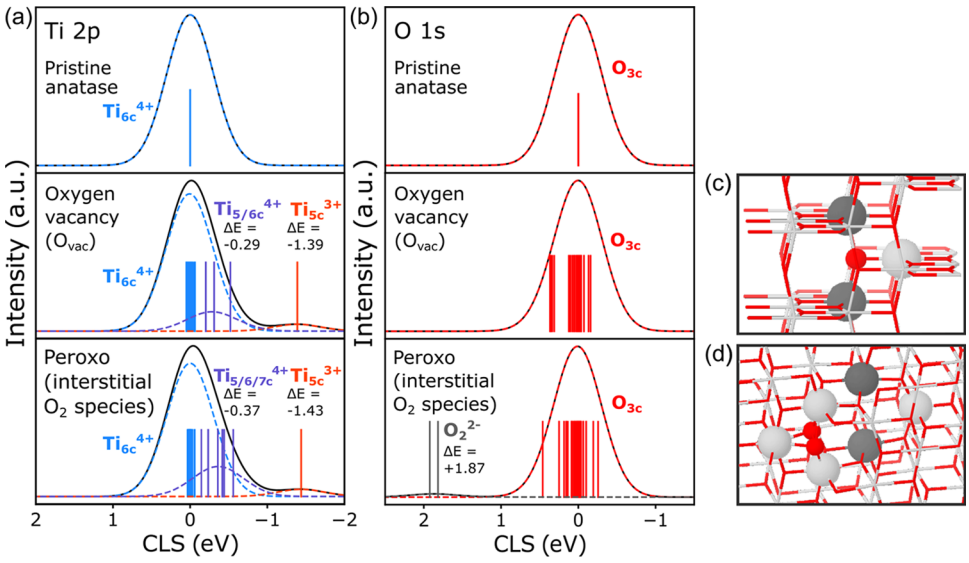

Figure 2. (a) Ti 2p and (b) O 1s core-level shifts of anatase TiO_2. The top row corresponds to pristine TiO_2, the middle row corresponds to TiO_2 with one oxygen vacancy, and the bottom row corresponds to an interstitial peroxo species containing TiO_2. The vertical lines indicate the CLS of individual atoms. (c) Pristine anatase bulk shows the oxygen atom that is removed to create the oxygen vacancy (red sphere) and the titanium atoms (gray spheres) coordinated to it. (d) Structure of the anatase bulk with interstitial peroxo species (red spheres) showing the Ti atoms (Ti_{7c}^{4+}) directly coordinated to the peroxo species and the three Ti atoms ($Ti_{5c}^{4+/3+}$) that surround the oxygen vacancy. Ti^{3+} ions are indicated by a darker shade of gray.

structure.[20,23] For the oxygen vacancy containing anatase, three groupings of peaks in the Ti 2p spectrum can be identified. Most Ti atoms in the bulk have CLS values within 0.11 eV of each other (blue peak labeled as Ti_{6c}^{4+}). These atoms are not directly connected to the created vacancy and are six-coordinated and have the same Bader charges as in the pristine bulk. The next group of shifts with lower binding energy are within 0.32 eV of each other, i.e., more spread out than the Ti_{6c}^{4+} peak. The maximum of the fitted Gaussian peak (violet peak labeled as $Ti_{5/6c}^{4+}$) is shifted by −0.29 eV from the Ti_{6c}^{4+} peak. There are six shifts in total, three at −0.12 eV, two at −0.22 eV, and one at −0.43 eV. The most negatively shifted value in the group comes from the pentacoordinated Ti_{5c} next to the oxygen vacancy, which accepts the least excess charge from the vacancy. The five others are Ti_{6c} atoms that are the next-nearest neighbors to the vacancy. The most negative shifts in the Ti 2p spectrum come from the two pentacoordinated Ti_{5c}^{3+} cations, where the excess electrons from the vacancy are localized. The peak (orange peak labeled as Ti_{5c}^{3+}) maximum is shifted by −1.39 eV compared to the Ti_{6c}^{4+} peak. The O 1s CLS of the oxygen vacancy containing anatase has two groups of values. Most oxygen atoms in the bulk have values within a range of 0.28 eV. Five oxygen anions give more positive values with the peak maximum (note: the fitted peak is not shown in Figure 2b) shifted by 0.36 eV compared to the main peak. These are oxygen anions that are the next-nearest neighbors to the vacancy and are in the same atomic layer as the vacancy.

In the third case, since the experimental XPS data show that amorphous titania retains a constant oxygen/titania ratio for increasing the ALD growth temperature (Figure S5), the possibility of having interstitial peroxo species in the anatase bulk was also investigated (see Figure 2d). The structure was generated by displacing one oxygen from its lattice position and placing it close to another oxygen. This creates an interstitial O_2 species (O_2^{2-}) connected to three heptacoordinated Ti_{7c} cations. The displaced oxygen leaves behind an oxygen vacancy with three pentacoordinated Ti_{5c} cations. The anatase structure with interstitial peroxo species has very similar Ti 2p shifts compared to anatase with an oxygen vacancy. The most negative Ti_{5c}^{3+} shift differs only by 0.04 eV, meaning that the oxygen vacancy created by the displacement of the lattice oxygen gives the same CLS signature as one created by the removal of oxygen. The main difference between the two spectra is the $Ti_{5/6/7c}^{4+}$ peak. The maximum of the fitted peak is shifted slightly more to the negative CLS for the peroxo structure (−0.37 eV). This is due to the fact that the three Ti_{7c}^{4+} cations that are coordinated to the peroxo species also have negative shifts compared to the ideal Ti_{6c}^{4+} further away from the defect sites. The O 1s spectrum of the peroxo anatase shows that the shifts of the oxygen anions are slightly more spread out than in the case of anatase with oxygen vacancy. In addition, the peroxo species gives a positive shift with a fitted peak maximum at +1.87 eV.

These computational results provide strong support for the proposed experimental XPS peak fitting (Figure 1), and especially, for identifying oxygen displacement-induced Ti^{4+} ions ($Ti_{5/6/7c}^{4+}$) from the spectra. In addition to the more negative shift of the $Ti_{5/6/7c}^{4+}$ peak (−0.37 eV) due to the interstitial peroxo species, oxygen vacancy formation via displacement of oxygen ions corresponds well with the experimentally determined rather stoichiometric and constant O/Ti ratio of 2. Albeit there are no remarkable differences between measured XPS O 1s spectra (Figure 1b), the slightly more distinct peak around 532 eV may imply more peroxo species in Ti^{3+}-rich am.-TiO_2 grown at 200 °C.

Besides anatase TiO_2, oxygen vacancy-induced core-level shifts in am.-TiO_2 were also computed. The calculated Ti 2p and O 1s core-level shifts for pristine and oxygen vacancy containing am.-TiO_2 (Figure S7) and the details of the analysis are presented in the Supporting Information. The Ti 2p shifts of pristine am.-TiO_2 are spread out but no obvious peak assignment correlating to the five-, six-, or seven-coordinated

https://doi.org/10.1021/acs.jpcc.1c10919
J. Phys. Chem. C 2022, 126, 4542−4554

Ti atoms can be made, i.e., the shifts do not correlate with the coordination number of the Ti atoms. Experimentally, this pristine amorphous phase should, in principle, give a broader peak than the anatase bulk due to the large spread of CLS. This is indeed observed in the experimental XPS Ti 2p data in Figure S6. Similarly, the O 1s shifts also span a broad range, with negative shifts showing slightly more separation between the shifts. For the oxygen vacancy containing am.-TiO_2, the shifts coming from five-, six-, and seven-coordinated Ti^{4+} cations are somewhat bunched together compared to the pristine bulk. The two Ti^{3+} cations have significant negative shifts, with the maximum of the fitted peak sitting at −1.37 eV. This is in quite good agreement with the assigned experimental Ti^{3+} peak, which is shifted by −1.7 eV compared to the anatase reference peak. Furthermore, despite the wide distribution of assorted $Ti_{5/6/7c}^{4+}$ core-level shifts that are not clearly correlating with any specific Ti ion bonding environment in am.-TiO_2, the computational peak fitting function was able to deconvolute two distinct $Ti_{5/6/7c}^{4+}$ peaks with CLS of −0.35 eV for oxygen vacancy containing am.-TiO_2 but not for pristine am.-TiO_2 (Figure S7). However, it should be noted that compared to computational results from anatase TiO_2, am.-TiO_2 is more challenging and the in-depth understanding of how a position of individual $Ti_{5/6/7c}^{4+}$ ion correlates with the observed CLS remains unclear.

Figure 3 presents the N 1s XP spectra of 30 nm thick ALD am.-TiO_2 deposited at different growth temperatures. Three

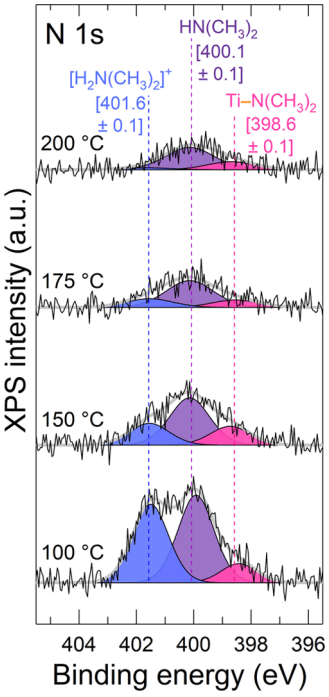

Figure 3. N 1s XP spectra of 30 nm thick ALD am.-TiO_2 grown at 100, 150, 175, and 200 °C.

nitrogen components were identified based on the surface reactions related to the TDMAT + H_2O process shown in eqs 5−7.[14,59]

$$Ti(OH)_2{}^* + Ti[N(CH_3)_2]_4 \rightarrow TiO_2{-}Ti[N(CH_3)_2]_2{}^* + 2HN(CH_3)_2 \quad (5)$$

$$TiO_2{-}Ti[N(CH_3)_2]_2{}^* + 2H_2O \rightarrow Ti(OH)_2{}^* + 2HN(CH_3)_2 \quad (6)$$

$$-OH^* + HN(CH_3)_2 \rightarrow -(O^-)[H_2N(CH_3)_2]^{+*} \quad (7)$$

The component at low binding energy (398.6 ± 0.1 eV) was assigned to unreacted Ti−$N(CH_3)_2$ bonds due to the incomplete TDMAT dissociation (eq 5).[14,60] Regarding ALD from TDMAT and H_2O, dissociation of TDMAT through the scission of the N−Ti bond is energetically more favorable than breaking of N−C bonds of the TDMAT molecule.[61] Moreover, dimethylamine ($N(CH_3)_2$) formation is preferred at growth temperatures <200 °C, whereas at higher temperatures decomposition of TDMAT and dimethylamine molecules leads to the increase of methane and carbon-containing species, i.e., carbon contamination in the coating.[62]

Consequently, the middle component most likely originates from trapped or re-adsorbed $HN(CH_3)_2$ reaction byproducts (eq 6), which can also react with surface −OH groups and form protonated $H_2N(CH_3)_2{}^+$ species (eq 7) causing the high binding energy peak in N 1s spectra.[14,59] Figure S8, showing the angle-resolved XPS (ARXPS) analysis of the N 1s spectrum for 30 nm thick as-deposited ALD am.-TiO_2 grown at 100 °C, confirms that the component at 400.1 eV has higher intensity with 60° photoelectron take-off angle, indicating the corresponding species to locate closer to the surface compared to the high binding energy (401.7 eV) N species. This further supports assigning the component at 400.1 eV to the $HN(CH_3)_2$ reaction byproducts instead of interstitial nitrogen, which is also known to appear around 400 eV.[63] The oxidized nitrogen species (Ti−N−O) can also have N 1s around 400 eV.[64,65] Although the Ti−N−O species cannot be completely excluded based on the N 1s binding energy alone, their presence is considered unlikely. The formation of oxidized nitrogen species would require the decomposition of the $HN(CH_3)_2$ product, which is stable up to 227 °C.[62]

The relative concentrations of titanium and nitrogen species as a function of the ALD growth temperature, presented in Figure 4, were obtained by a quantitative analysis of the XP spectra. Figure 4a shows that as the growth temperature is increased, the concentrations of Ti^{3+} and oxygen displacement-induced Ti^{4+} ions ($Ti_{5/6/7c}^{4+}$) steadily increase, simultaneously with the decreasing number of Ti_{6c}^{4+} ions, and when the growth temperature of 150 °C is exceeded, >50% concentration of O ions displacement-mediated titanium defects (Ti^{3+} + $Ti_{5/6/7c}^{4+}$) starts to dominate the amorphous titania structure. At the growth temperature of 200 °C, the amount of Ti^{3+} defects is more than double compared to am.-TiO_2 grown at 100 °C. The results are also concordant with the theory that the concentration of $Ti_{5/6/7c}^{4+}$ ions increases together with the Ti^{3+} defects since they both arise due to the displacement of oxygen ions in the am.-TiO_2 structure.[20,23]

Deskins et al. used classical molecular dynamics to study amorphous TiO_x with different stoichiometries and calculated the probabilities of Ti^{4+}−O−Ti^{4+} and Ti^{3+}−O−Ti^{3+} linkages and average Ti^{4+}/Ti^{4+} and Ti^{3+}/Ti^{3+} distances.[4] There are always two Ti^{3+} ions involved in the Ti^{3+}−O−Ti^{3+} bond structure but because Ti^{4+}−O−Ti^{3+} connections also exist, the concentration of Ti^{3+} defects cannot be directly calculated by multiplying the probability by 2. Consequently, concerning the experimental results shown in Figure 4a, the am.-TiO_2 deposited at 100 °C (Ti^{3+}/Ti_{tot} = 12%) may have Ti^{3+}−O−

https://doi.org/10.1021/acs.jpcc.1c10919
J. Phys. Chem. C 2022, 126, 4542−4554

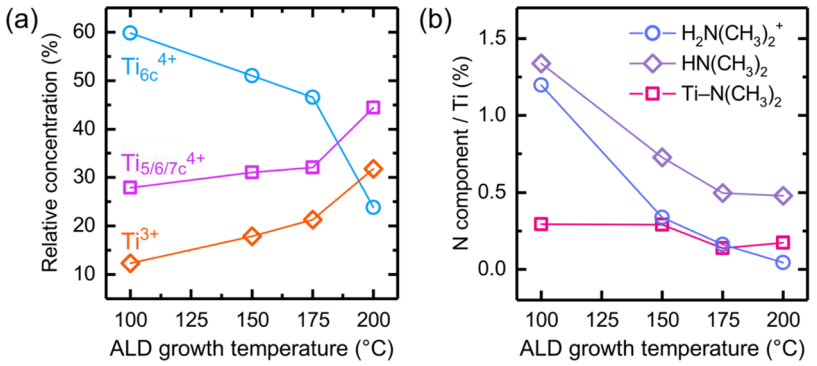

Figure 4. XPS analysis of (a) Ti and (b) N components for 30 nm thick ALD am.-TiO_2 grown at 100, 150, 175, and 200 °C.

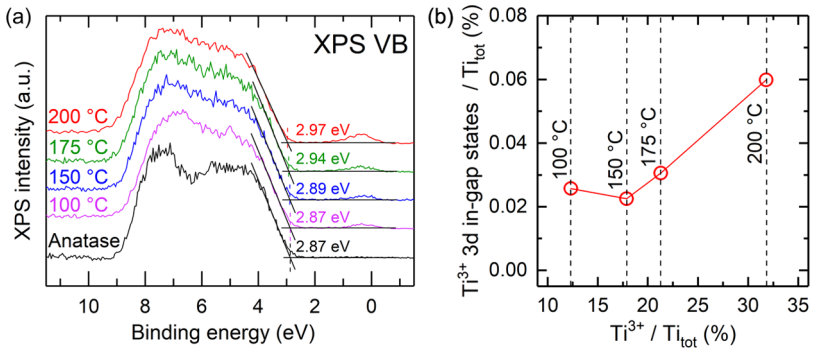

Figure 5. (a) VB XP spectra of 30 nm thick ALD am.-TiO_2 grown at 100, 150, 175, and 200 °C. Anatase TiO_2(30 nm) is shown as a reference for defect-free crystalline TiO_2. (b) The relative in-gap state concentration as a function of Ti^{3+} concentration for 30 nm thick ALD am.-TiO_2 grown at 100, 150, 175, and 200 °C.

Ti^{3+} linkage probability even less than 0.05, which, based on the work by Deskins et al., corresponds with am.-$TiO_{1.90-2.00}$ and average Ti^{3+}/Ti^{3+} distance of 3−7 Å. By contrast, am.-TiO_2 deposited at 200 °C (Ti^{3+}/Ti_{tot} = 32%) exhibits most likely higher Ti^{3+}−O−Ti^{3+} linkage probability and thus average Ti^{3+}/Ti^{3+} distance around 3 Å, which is the minimum distance within am.-TiO_2.[4] These differences in the hopping distance were suggested to explain enhanced hole conduction in am.-TiO_2 with a higher Ti^{3+} defect concentration.[4] Despite the fact that in this work, the O/Ti ratio of am.-TiO_2 thin films is close to 2 (Figure S5), and Deskins et al. studied amorphous titania with different stoichiometries, both studies involve similar phenomena and Ti^{3+} defects within am.-TiO_2.[4]

Regarding nitrogen impurities as a function of ALD growth temperature shown in Figure 4b, the concentrations of TDMAT fragments, i.e., $HN(CH_3)_2$ and $H_2N(CH_3)_2^+$ species, are clearly higher in am.-TiO_2 grown at 100 °C than at 150−200 °C, whereas the amount of unreacted Ti−$N(CH_3)_2$ remains rather constant. This is probably due to the slower desorption or re-adsorption of the reaction byproducts during the ALD growth at lower growth temperatures, albeit there are still some trapped $HN(CH_3)_2$ in am.-TiO_2 deposited at 200 °C. Based on the relative concentrations of elements of the am.-TiO_2 samples shown in Table S3, all of the samples contain also some carbon impurities (3−5 atom %). It is, however, not feasible to differentiate these species from adventitious carbon that results from the sample transfer between the ALD chamber and the XPS system.

To acquire a deeper understanding of how titanium and nitrogen defects influence the in-gap states, the XPS valence band (VB) spectra of am.-TiO_2 grown at 100, 150, 175, and 200 °C were measured. The analysis of XPS valence band spectra in Figure 5a reveals an in-gap state in the binding energy range of 0.3−0.4 eV, which can be assigned to the Ti^{3+} 3d electronic state.[28,31] Similar defect state is also seen in the computational density of state analysis when oxygen vacancy is introduced in the anatase TiO_2 lattice (Figure S9). Accordingly, the intensity of the in-gap state increases linearly with the Ti^{3+} concentration determined from the Ti 2p transition between growth temperatures of 150 and 200 °C. At 100 °C, some deviation from the trend is observed (Figure 5b). This deviation is likely due to the high amount of nitrogen species within the 100 °C grown am.-TiO_2, which may also introduce the density of states within the band gap.[66] Nevertheless, the observed in-gap state peak is clearly mainly induced by the Ti^{3+} defects and not by the N species. The anatase TiO_2 reference does not have any Ti^{3+} and shows no in-gap state. An attempt was made to measure in-gap states with ultraviolet photoelectron spectroscopy (UPS) but the peak was not clearly resolved (Figure S10). The UPS VB measurement is more surface sensitive than the XPS VB measurement due to much lower photoelectron energies (15 vs 1480 eV).[67] Thus, the apparent discrepancy is likely due to the surface effects, either impurities or difference in surface vs bulk composition. Previously, we observed the onset of the $Ti^{3+/2+}$ 3d peak at 0.72−0.50 eV in the UPS data only after annealing at 400 °C in a vacuum despite the presence of $Ti^{3+/2+}$ species in the as-deposited ALD am.-TiO_2 thin film, and the onset coincided with the removal of adventitious contamination.[19]

To understand how the Ti^{3+}-mediated defect states influence the properties of am.-TiO_2, steady-state absorbance, transient absorption spectroscopy, and electrical conductivity measurements were carried out. Steady-state absorbance

https://doi.org/10.1021/acs.jpcc.1c10919
J. Phys. Chem. C 2022, 126, 4542−4554

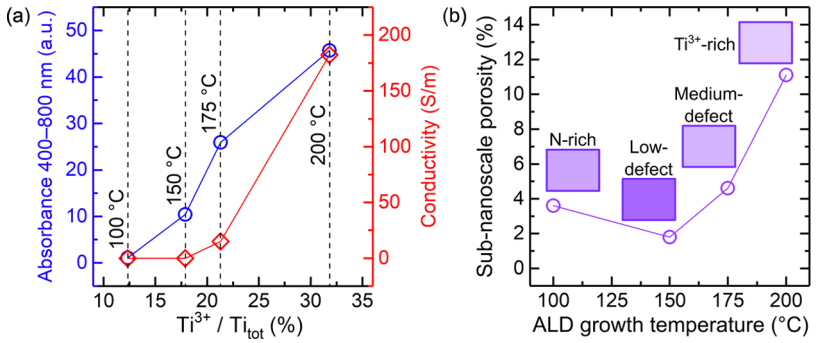

Figure 6. (a) Integrated absorbance in the visible range and electrical conductivity and (b) sub-nanoscale porosity of 30 nm thick ALD am.-TiO_2 grown at 100, 150, 175, and 200 °C.

spectra in the UV−vis range are presented in Figure S11a, and further analysis of the optical band gap is shown in Figure S11b. The results in Figure S11a show increasing visible-light absorption with increasing ALD TiO_2 growth temperature. Here, visible-light absorption is caused by the Ti^{3+} defects that have energy states within the band gap. The broader UV−NIR range absorption measurement presented in Figure S12 revealed that the 200 °C grown ALD am.-TiO_2 has a broad Ti^{3+} 3d defect-mediated absorption band within the band gap with a maximum at 937 nm (1.32 eV) and the defect band edge at 0.24 eV (5200 nm). The small amount of Ti^{3+} 3d defect states in the 100 °C grown ALD am.-TiO_2 is not sufficient to form a defect band-like absorption. The main absorption edge of amorphous TiO_2 is less steep compared to crystalline TiO_2[68] due to the tailing of electronic states into the band gap.[3,12,69,70] Although the visible-light absorption was strongly affected by the growth temperature, only a subtle increase from 3.53 to 3.61 eV was observed in the optical band gap (Figure S11b) and concurrent shift (0.1 eV) toward higher binding energies was observed in the XPS VB edge position (Figure 5a), suggesting a slight widening of the band gap. Interestingly, the band gap values were large compared to those of the bulk anatase TiO_2 (3.2 eV) and 30 nm thick anatase TiO_2 thin film (3.4 eV).[35] Such a blue-shift could have been caused by the quantum confinement effects,[71] while the band gap broadening with ALD growth temperature could be induced by the high concentration of Ti^{3+} states giving rise to the Moss−Burstein effect.[12,72] It has been proposed that due to the shallow nature of Ti^{3+} defect states, the electrons could be excited thermally to the conduction band (CB) and induce free carrier absorption and electronic conductivity.[20,73] However, the observed defect band edge at 0.24 eV shows that the band does not reach the conduction band and thermal excitation is unlikely.

In contrast to the growth temperatures of 150−200 °C, am.-TiO_2 grown at 100 °C showed only little absorption for the wavelengths above 350 nm. Especially, features at 400−500 nm associated with substitutional N-doping[65,74] were not observed (Figure S11a, inset). This suggests that the nitrogen precursor traces, mainly present in the 100 °C grown ALD am.-TiO_2, do not induce absorption in the visible range, and furthermore, with only a low concentration of Ti^{3+}, the thin film can be considered transparent to the visible light.

Figure 6a emphasizes the relation between visible range absorbance and Ti^{3+} defects by presenting the integrated absorbance in the wavelength range of 400−800 nm as a function of relative Ti^{3+} ion concentration. We note that the absorption band has the maximum outside the visible range at 937 nm but the integrated area is proportional to the absorption band area. Am.-TiO_2 grown at 100 °C shows only minor visible-light absorption and has the lowest Ti^{3+} concentration (Ti^{3+}/Ti_{tot} = 12%). Then, the visible range absorption increases with the concentration of Ti^{3+} defects. Compared to the visible range absorbance, electrical conductivity starts to increase steeply after 20% Ti^{3+}/Ti_{tot} concentration is reached (Figure 6a). The observed electrical conductivity corresponds to the computationally studied polaron hopping mechanism, which is strongly related to the unpaired electrons of Ti^{3+} defects and distances between adjacent Ti^{3+} ions, as discussed also earlier in this work.[4,7,20,25] Furthermore, this is supported by Nunez et al., who found a correlation between the concentration of Ti^{3+} and conductivity by comparing ALD TiO_2 grown using either TDMAT or $TiCl_4$ precursors.[21] They stated that the conductivity of TiO_2 thin films is consistent with the hopping mechanism, instead of conduction via the conduction or valence bands.[21] The hopping mechanism also explains the differences in the onsets of visible-light absorption and conductivity. Thus, around 20% Ti^{3+}/Ti_{tot} concentration is needed for a sufficient amount of unpaired electrons and proximity of Ti^{3+} ions for continuous electron flow through defect pathways to induce electrical conductivity, whereas visible-light absorption occurs with lower Ti^{3+}/Ti_{tot} concentration since it depends only on the concentration of occupied Ti^{3+} 3d in-gap states and is not affected by the average distances of Ti^{3+} ions. With a high enough Ti^{3+} concentration, as in the case of the 200 °C grown am.-TiO_2, the Ti^{3+} 3d states overlap sufficiently for delocalization and form a defect band responsible for the increased electrical conductivity. This defect band does not however reach the conduction band, and therefore, the conduction mechanism via free (delocalized) electrons in the conduction band is not supported.

Ellipsometer measurements (Figure S13) revealed a significant change in the refractive index of am.-TiO_2 as the ALD growth temperature was changed. In general, a higher refractive index can be interpreted as a higher density material and, for example, for titania, the refractive index is reported to vary between 2.1 and 2.9 depending on the phase and the density of TiO_2: am.-TiO_2 (2.1−2.4), anatase TiO_2 (2.4−2.5) and rutile TiO_2 (2.8−2.9).[58,75,76] Thus, we propose that the observed differences in the refractive indices are due to the sub-nanoscale porosity within the am.-TiO_2 structure being the highest for am.-TiO_2 grown at 200 °C. The sub-nanoscale porosity of ALD am.-TiO_2 modeled by the Lorentz−Lorenz effective medium approximation (EMA) is presented in Figure 6b. The same model was also used earlier by Dufond et al. to

https://doi.org/10.1021/acs.jpcc.1c10919
J. Phys. Chem. C 2022, 126, 4542−4554

study the effect of ligands within ALD am.-TiO_2 grown using titanium isopropoxide (TTIP) and H_2O as ALD precursors.[58] Based on the modeling and the results in Figure 6b, the am.-TiO_2 grown at 150 °C is the most dense (n = 2.35, p = 2%), likely due to the rather low concentration of both nitrogen and titanium defects. The Am.-TiO_2 grown at 100 °C, instead, includes N-bearing TDMAT fragments that decrease the packing density of am.-TiO_2 leading to a slightly higher sub-nanoscale porosity of around 4%. Increasing the ALD growth temperature to >150 °C results in more oxygen displacement-induced Ti^{4+} ions ($Ti_{5/6/7c}^{4+}$) and Ti^{3+} defects that imply the formation of oxygen vacancies, i.e., local sub-nanoscale porosity within am.-TiO_2. Therefore, the Ti^{3+}-rich am.-TiO_2 grown at 200 °C exhibits the lowest refractive index of 2.14, corresponding to the sub-nanoscale porosity of 11%.

In addition to the refractive index, Figure S13 shows the ALD growth per cycle (GPC) calculated by dividing the thin film thickness by the number of ALD cycles. There is a distinct decrease in the GPC, as the ALD growth temperature is increased from 100 to 200 °C. Some reasons for lower GPC are proposed to be attributed to slower adsorption of TDMAT or intermediate product desorption.[16,60] It should be also noticed that the thermal decomposition of TDMAT may affect the self-limiting ALD process at 200 °C.[16] We consider that, possibly, the intermediate product desorption and nonideal ALD process at 200 °C are the reasons for the observed unprecedented Ti^{3+}-rich nature and sub-nanoscale porosity of our ALD am.-TiO_2 grown at 200 °C.[16]

Transient absorption spectroscopy (TAS) was carried out to study the charge carrier dynamics in am.-TiO_2 thin films. am.-TiO_2 samples were excited at 320 nm and monitored at 410−1250 nm (3.0−1.0 eV). The excitation (pump) energy used was 60 $\mu J/cm^2$. The excitation wavelength was chosen to match the band gap absorption (Figure S11a), i.e., to excite electrons from the valence band to the conduction band, but it also excites electrons from any band gap state to the conduction band.

Two types of responses were observed depending on the am.-TiO_2 deposition temperature. The positive broad absorbance band with a maximum in the 600−800 nm range was recorded for am.-TiO_2 deposited at 100 °C (Figure S14) and 150 °C (Figure S15). This response can be assigned to the carriers in the CB or to the carriers, either holes or electrons, trapped to the in-gap states 1.5−2.5 eV above the valence band.[68] The carrier lifetimes for 100−150 °C grown am.-TiO_2 were extremely short, less than 10 ps, as presented in Figure 7. Quite surprisingly, this broadband response is similar to crystalline TiO_2 thin films with the exception that in crystalline TiO_2 the carrier lifetimes are in the nanosecond range.[68] The short carrier lifetime indicates fast recombination of trapped charge carriers in am.-TiO_2 and is assigned to its defective nature.[35] Indeed, the XPS VB spectra (Figure 5a) show an increased amount of band gap states for all of the am.-TiO_2 compared to the crystalline TiO_2 reference. On the contrary, for 200 °C grown am.-TiO_2, the response is negative (Figure S17), and arises from bleaching of the ground state absorption in the visible and NIR range.[77] Yet, the response (ΔA) was still of broad band nature in the 600−800 nm range. Since the origin of the ground-state absorption is the transition from the VB and in-gap states to the CB, the explanation for the observation is the excitation of the electrons of in-gap states by the pump pulse. This transition gives rather a long lifetime of the charge carriers, extended to the ns time scale. The am.-TiO_2 deposited at 175 °C (Figure S16) presents an intermediate case when both types of responses were observed simultaneously, a fast decay of the positive response (fast recombination of the carriers in the CB) characteristic for am.-TiO_2 and slow relaxation of the ground-state absorption bleaching (relaxation of the electrons back to the in-gap states) exhibited by Ti^{3+}-rich "black" am.-TiO_2.

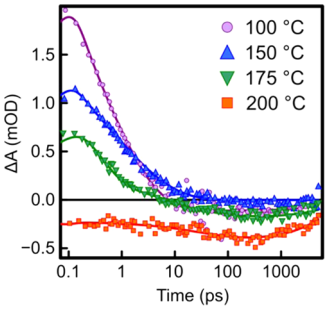

Figure 7. TAS decay spectra at 750 nm (1.65 eV) in the picosecond time domain of 30 nm thick amorphous ALD am.-TiO_2 grown at 100, 150, 175, and 200 °C.

The carrier lifetime of the 200 °C grown am.-TiO_2 is similar to the crystalline TiO_2.[68] This is at first surprising since the carrier lifetime is known to increase with amorphous to crystalline transition due to the decrease in the amount of oxide defects and trap states. The "black" am.-TiO_2 grown at 200 °C is loaded with oxide defects, and one would expect carrier lifetimes to become even shorter due to the fast recombination at the oxide defects and trap states. We have to bear in mind that the 200 °C grown "black" am.-TiO_2 thin film has an exceptionally high concentration of Ti^{3+} defects that seem to correlate with the extended carrier lifetime. The long carrier lifetime indicates slow recombination of charge carriers, which indicates a decrease in the amount of trap states. Thus, it seems plausible that Ti^{3+} defects fill trap states responsible for the carrier recombination. In the case of 200 °C grown am.-TiO_2, these trap states are fully occupied resulting in an increased carrier lifetime. In a broader context, carrier lifetimes can be increased either by removing defects and trap states, i.e., crystalline TiO_2 or by saturating the material with defects, as was shown here for "black" am.-TiO_2 grown at 200 °C.

Vequizo et al. presented a photodynamic mechanism of photogenerated electrons in nonreduced and reduced $SrTiO_3$ photocatalysts.[33] In nonreduced $SrTiO_3$ with a minor amount of oxygen vacancies and Ti^{3+} defects, electrons can be deeply trapped at the intrinsic in-gap states after the pump pulse and then subsequently be excited to the conduction band by absorbing vis−NIR light. However, in reduced and Ti^{3+}-rich $SrTiO_3$, in-gap states are already occupied by electrons leading to an extended lifetime of charge carriers photoexcited by the pump pulse and absorption of lower energy IR photons by electrons at shallow trap states.[33] Our proposed mechanism for the extended carrier lifetime of 200 °C grown am.-TiO_2 with an also high degree of Ti^{3+} defects is in accordance with this model, albeit our probe range was limited to >1 eV transitions.

To assess the contribution of TDMAT fragments to the carrier dynamics, a comparison was made with amorphous TiO_2 grown by the ion-beam sputtering (IBS) method. The IBS am.-TiO_2 does not contain any nitrogen impurities but Ti 2p is similar to ALD am.-TiO_2 grown at 100 °C (Figure S18), indicating low Ti^{3+} concentration and lattice disorder-mediated

https://doi.org/10.1021/acs.jpcc.1c10919
J. Phys. Chem. C 2022, 126, 4542−4554

broadening of the Ti^{4+} peak compared to the crystalline TiO_2. The TA spectra of IBS am.-TiO_2 were found to be similar to the ALD am.-TiO_2 grown at 100 °C (Figure S19) but the carriers had more than ten times longer lifetimes (>100 ps). This suggests that even though the TA spectra are not affected by the N-bearing TDMAT fragments in the am.-TiO_2 thin film, they may still contribute to carrier trapping. The similarity of Ti 2p spectra recorded for the amorphous IBS TiO_2 and ALD TiO_2 thin films in Figure S18a also indicates generality of the proposed component analysis, where in addition to hexacoordinated (Ti_{6c}^{4+}) ions, penta- and heptacoordinated ($Ti_{5/7c}^{4+}$) ions are also required to fit the Ti 2p spectrum of amorphous IBS TiO_2.

As reported by Khan et al., conversion from the am.-TiO_2 to polycrystalline anatase phase leads to a strong increase in carrier lifetimes, from ps to ns range,[35] which can be now experimentally rationalized by the absence of penta- and heptacoordinated ($Ti_{5/7c}^{4+}$) ions in crystalline TiO_2 that are, on the contrary, rather common in am.-TiO_2.[3−5] The Ti^{3+} 3d in-gap state is also removed upon oxidation but is not responsible for the short carrier lifetimes. Conversely, the introduction of high Ti^{3+} concentration to the am.-TiO_2 was followed by carrier lifetimes similar to the polycrystalline TiO_2. On the other hand, our results suggest that N-bearing TDMAT fragments in the am.-TiO_2 thin film could contribute to the short carrier lifetimes acting as carrier traps.

The schematic illustration in Figure 8 summarizes the ALD growth temperature-induced controllability of Ti^{3+} defects

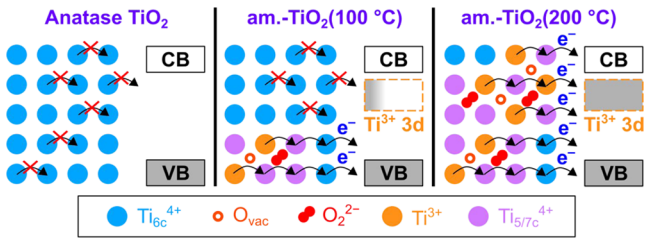

Figure 8. Schematic illustration of electrical conduction in am.-TiO_2 by the polaron hopping mechanism. Ti^{3+} defects in am.-TiO_2 populate the Ti 3d state within the band gap with an excess charge carrier polaron that can "hop" from a Ti^{3+} site to a Ti^{4+} site, i.e., Ti^{3+}−Ti^{4+} ↔ Ti^{4+}−Ti^{3+}. Pure anatase TiO_2 does not have any electronic state within the band gap and no Ti^{3+} defects to initiate electron hopping. Conductivity scales with the Ti^{3+} concentration can be controlled with ALD growth temperature. With increasing Ti^{3+} concentration, the Ti^{3+} 3d states within the band gap become close enough and form a defect band. By common theory, an oxygen vacancy, O_{vac}, generates two Ti^{3+} sites and decreases the coordination of neighboring Ti^{4+} cations. Furthermore, the O ion that formed O_{vac} can bond with another oxygen creating an interstitial O_2 species (O_2^{2-}) connected to three heptacoordinated Ti_{7c} cations. Amorphous TiO_2 is rich in under- and overcoordinated $Ti_{5/7c}$ cations, whereas crystalline TiO_2 consists of only six-coordinated (Ti_{6c}) cations.

within am.-TiO_2 and their effect on the electrical conduction mechanism. From the PEC application point of view, comprehensive research regarding tunable charge carrier dynamics, absorption, and electrical "leakiness" of ALD am.-TiO_2 presented in this work provides a better understanding of possible tailoring of properties related to protective ALD am.-TiO_2 photoelectrode coatings made of nonconductive or degenerated/intrinsically "leaky" amorphous ALD am.-TiO_2 grown using TDMAT and H_2O precursors.[6,78−80] Furthermore, the controllable and direct synthesis of "black" am.-TiO_2 via atomic layer deposition is of wide interest in photocatalyst applications,[7,9,10] whereas low conductivity of low-temperature grown am.-TiO_2 may be applied as a high-κ dielectric.[81,82] Such a diversity in the properties of amorphous titania could also provide an interesting approach to area-selective ALD, e.g., by possible differences in adsorption of self-assembled monolayers (SAMs) or preferential growth of metallic or oxide materials on conductive (high density of donor defects) and nonconductive (low density of donor defects) substrates.[83,84]

CONCLUSIONS

In summary, a comprehensive electron and optical absorption spectroscopy study were conducted for atomic layer deposited am.-TiO_2 to provide insights into the amorphous structure of titania and its charge carrier dynamics. The correlation between our electron spectroscopy results and a first-principles core-level shift analysis allowed us to differentiate penta- and heptacoordinated ($Ti_{5/7c}^{4+}$) ions, induced by oxygen vacancies and interstitial peroxo species within the amorphous TiO_2 structure. The formation of Ti^{3+} defects was found to induce a chemical shift to the Ti^{4+} 2p core-level spectrum of am.-TiO_2, which could not be explained by the structural disorder alone. Furthermore, we showed that Ti^{3+} and nitrogen defects in am.-TiO_2 can be tailored in a controlled and elegant manner via tuning the ALD growth temperature between 100 and 200 °C when using TDMAT and H_2O as the precursors. The lower deposition temperature results in nitrogen-bearing precursor traces within the am.-TiO_2, whereas the higher growth temperature leads to increased concentration of Ti^{3+} and oxygen displacement-induced Ti^{4+} ions ($Ti_{5/6/7c}^{4+}$).

The am.-TiO_2 grown at 100 °C shows no visible-light absorption but after the Ti^{3+} concentration (Ti^{3+}/Ti_{tot}) exceeds ∼12%, the visible light absorption increases with the amount of Ti^{3+} defects resulting in "black" am.-TiO_2 at ALD growth temperature of 200 °C. The onset of electrical conductivity requires >20% Ti^{3+}/Ti_{tot}, and the conductivity mechanism was identified as polaron hopping-induced conductivity. The transient absorption (TA) response of am.-TiO_2 grown at 100 °C was similar to crystalline TiO_2 in terms of the TA spectrum but the carrier lifetime was only <10 ps (vs few ns for crystalline TiO_2) due to the amorphous structure. In contrast, the high concentration of Ti^{3+} defects in "black" am.-TiO_2 was shown to decrease the recombination rate and thereby increase the carrier lifetime to the nanosecond time domain, which is comparable to the crystalline low-defect TiO_2. Nitrogen traces from the TDMAT precursor, on the other hand, had no remarkable effect on either the optical or the charge transfer properties.

These results provide new atomic-level insights into the formation and controlling of intrinsic Ti^{3+} defects in ALD grown am.-TiO_2. The ALD grown am.-TiO_2 has stoichiometric composition despite the high (up to 33%) Ti^{3+} concentration, which is explained by the formation of interstitial peroxo species with oxygen vacancies. The Ti^{3+} defects mediate the enhanced charge transfer of am.-TiO_2 that is a critical parameter in the optimization of ALD TiO_2-based protective photoelectrode coatings in photoelectrochemical solar fuel reactors.

https://doi.org/10.1021/acs.jpcc.1c10919
J. Phys. Chem. C 2022, 126, 4542−4554

■ ASSOCIATED CONTENT

Supporting Information

The Supporting Information is available free of charge at https://pubs.acs.org/doi/10.1021/acs.jpcc.1c10919.

Details of the computational method; the effect of applied *U*-value; details on the formation of oxygen vacancies and peroxo species; results for am.-TiO_2; GIXRD measurements; and XPS, UPS, steady-state UV−vis−NIR spectroscopy, ellipsometry, and transient absorption spectroscopy (PDF)

■ AUTHOR INFORMATION

Corresponding Authors

Harri Ali-Löytty − *Surface Science Group, Faculty of Engineering and Natural Sciences, Tampere University, FI-33014 Tampere, Finland;* orcid.org/0000-0001-8746-7268; Email: harri.ali-loytty@tuni.fi

Mika Valden − *Surface Science Group, Faculty of Engineering and Natural Sciences, Tampere University, FI-33014 Tampere, Finland*; Email: mika.valden@tuni.fi

Authors

Jesse Saari − *Surface Science Group, Faculty of Engineering and Natural Sciences, Tampere University, FI-33014 Tampere, Finland;* orcid.org/0000-0001-6741-0838

Minttu Maria Kauppinen − *Competence Centre for Catalysis and Department of Physics, Chalmers University of Technology, SE-412 96 Göteborg, Sweden*

Markku Hannula − *Surface Science Group, Faculty of Engineering and Natural Sciences, Tampere University, FI-33014 Tampere, Finland;* orcid.org/0000-0003-1110-7439

Ramsha Khan − *Photonic Compounds and Nanomaterials Group, Faculty of Engineering and Natural Sciences, Tampere University, FI-33014 Tampere, Finland*

Kimmo Lahtonen − *Faculty of Engineering and Natural Sciences, Tampere University, FI-33014 Tampere, Finland;* orcid.org/0000-0002-8138-7918

Lauri Palmolahti − *Surface Science Group, Faculty of Engineering and Natural Sciences, Tampere University, FI-33014 Tampere, Finland;* orcid.org/0000-0001-9992-6628

Antti Tukiainen − *Faculty of Engineering and Natural Sciences, Tampere University, FI-33014 Tampere, Finland*

Henrik Grönbeck − *Competence Centre for Catalysis and Department of Physics, Chalmers University of Technology, SE-412 96 Göteborg, Sweden*

Nikolai V. Tkachenko − *Photonic Compounds and Nanomaterials Group, Faculty of Engineering and Natural Sciences, Tampere University, FI-33014 Tampere, Finland;* orcid.org/0000-0002-8504-2335

Complete contact information is available at: https://pubs.acs.org/10.1021/acs.jpcc.1c10919

Notes

The authors declare no competing financial interest.

■ ACKNOWLEDGMENTS

The authors thank Aleksi Tikka for UV−NIR measurements and Riina Ulkuniemi for conductivity and UV−vis measurements. The authors also thank David Mora-Fonz and Alexander L. Shluger for providing structural models for amorphous titania. Financial support is acknowledged from the Knut and Alice Wallenberg Foundation. The calculations were performed at C3SE via a SNIC grant. This work is part of the Academy of Finland Flagship Programme, Photonics Research and Innovation (PREIN) (Decision Number 320165) and was supported by the Academy of Finland (Decision Numbers 326461, 326406), by Jane & Aatos Erkko Foundation (Project "Solar Fuels Synthesis"), and by Business Finland (TUTLi project "Liquid Sun") (Decision Number 1464/31/2019). J.S. was supported by The Vilho, Yrjö, and Kalle Väisälä Foundation of the Finnish Academy of Science and Letters and L.P. by KAUTE Foundation. R.K. acknowledges the Doctoral program of Tampere University.

■ REFERENCES

(1) Fujishima, A.; Honda, K. Electrochemical Photolysis of Water at a Semiconductor Electrode. *Nature* **1972**, *238*, 37−38.

(2) Pelaez, M.; Nolan, N. T.; Pillai, S. C.; Seery, M. K.; Falaras, P.; Kontos, A. G.; Dunlop, P. S. M.; Hamilton, J. W. J.; Byrne, J. A.; O'Shea, K.; et al. Review on the Visible Light Active Titanium Dioxide Photocatalysts for Environmental Applications. *Appl. Catal., B* **2012**, *125*, 331−349.

(3) Prasai, B.; Cai, B.; Underwood, M. K.; Lewis, J. P.; Drabold, D. A. Properties of Amorphous and Crystalline Titanium Dioxide from First Principles. *J. Mater. Sci.* **2012**, *47*, 7515−7521.

(4) Deskins, N. A.; Du, J.; Rao, P. The Structural and Electronic Properties of Reduced Amorphous Titania. *Phys. Chem. Chem. Phys.* **2017**, *19*, 18671−18684.

(5) Mora-Fonz, D.; Kaviani, M.; Shluger, A. L. Disorder-Induced Electron and Hole Trapping in Amorphous TiO_2. *Phys. Rev. B* **2020**, *102*, No. 054205.

(6) Hu, S.; Shaner, M. R.; Beardslee, J. A.; Lichterman, M.; Brunschwig, B. S.; Lewis, N. S. Amorphous TiO_2 Coatings Stabilize Si, GaAs, and GaP Photoanodes for Efficient Water Oxidation. *Science* **2014**, *344*, 1005−1009.

(7) Glezakou, V.-A.; Rousseau, R. Shedding Light on Black Titania. *Nat. Mater.* **2018**, *17*, 856−857.

(8) Sivula, K. Defects Give New Life to an Old Material: Electronically Leaky Titania as a Photoanode Protection Layer. *ChemCatChem* **2014**, *6*, 2796−2797.

(9) Liu, X.; Zhu, G.; Wang, X.; Yuan, X.; Lin, T.; Huang, F. Progress in Black Titania: A New Material for Advanced Photocatalysis. *Adv. Energy Mater.* **2016**, *6*, No. 1600452.

(10) Chen, X.; Liu, L.; Huang, F. Black Titanium Dioxide (TiO_2) Nanomaterials. *Chem. Soc. Rev.* **2015**, *44*, 1861−1885.

(11) Dendooven, J.; Detavernier, C. In *Atomic Layer Deposition in Energy Conversion Applications*; Bachmann, J., Ed.; John Wiley & Sons, Ltd., 2017; pp 1−40.

(12) Ali-Löytty, H.; Hannula, M.; Saari, J.; Palmolahti, L.; Bhuskute, B. D.; Ulkuniemi, R.; Nyyssönen, T.; Lahtonen, K.; Valden, M. Diversity of TiO_2: Controlling the Molecular and Electronic Structure of Atomic-Layer-Deposited Black TiO_2. *ACS Appl. Mater. Interfaces* **2019**, *11*, 2758−2762.

(13) Reiners, M.; Xu, K.; Aslam, N.; Devi, A.; Waser, R.; Hoffmann-Eifert, S. Growth and Crystallization of TiO_2 Thin Films by Atomic Layer Deposition Using a Novel Amido Guanidinate Titanium Source and Tetrakis-Dimethylamido-Titanium. *Chem. Mater.* **2013**, *25*, 2934−2943.

(14) Head, A. R.; Chaudhary, S.; Olivieri, G.; Bournel, F.; Andersen, J. N.; Rochet, F.; Gallet, J.-J.; Schnadt, J. Near Ambient Pressure X-Ray Photoelectron Spectroscopy Study of the Atomic Layer Deposition of TiO_2 on RuO_2(110). *J. Phys. Chem. C* **2016**, *120*, 243−251.

(15) Kääriäinen, T.; Cameron, D.; Kääriäinen, M.-L.; Sherman, A. *Atomic Layer Deposition: Principles, Characteristics, and Nanotechnology Applications*, 2nd ed.; Scrivener Publishing: Beverly, MA, 2013.

(16) Xie, Q.; Jiang, Y.-L.; Detavernier, C.; Deduytsche, D.; Van Meirhaeghe, R. L.; Ru, G.-P.; Li, B.-Z.; Qu, X.-P. Atomic Layer Deposition of TiO_2 from Tetrakis-Dimethyl-Amido Titanium or Ti Isopropoxide Precursors and H_2O. *J. Appl. Phys.* **2007**, *102*, No. 083521.
(17) McDowell, M. T.; Lichterman, M. F.; Carim, A. I.; Liu, R.; Hu, S.; Brunschwig, B. S.; Lewis, N. S. The Influence of Structure and Processing on the Behavior of TiO_2 Protective Layers for Stabilization of n-Si/TiO_2/Ni Photoanodes for Water Oxidation. *ACS Appl. Mater. Interfaces* **2015**, *7*, 15189−15199.
(18) Deng, S.; Verbruggen, S. W.; Lenaerts, S.; Martens, J. A.; Van den Berghe, S.; Devloo-Casier, K.; Devulder, W.; Dendooven, J.; Deduytsche, D.; Detavernier, C. Controllable Nitrogen Doping in as Deposited TiO_2 Film and Its Effect on Post Deposition Annealing. *J. Vac. Sci. Technol., A* **2013**, *32*, No. 01A123.
(19) Hannula, M.; Ali-Löytty, H.; Lahtonen, K.; Sarlin, E.; Saari, J.; Valden, M. Improved Stability of Atomic Layer Deposited Amorphous TiO_2 Photoelectrode Coatings by Thermally Induced Oxygen Defects. *Chem. Mater.* **2018**, *30*, 1199−1208.
(20) Di Valentin, C.; Pacchioni, G.; Selloni, A. Reduced and n-Type Doped TiO_2: Nature of Ti^{3+} Species. *J. Phys. Chem. C* **2009**, *113*, 20543−20552.
(21) Nunez, P.; Richter, M. H.; Piercy, B. D.; Roske, C. W.; Cabán-Acevedo, M.; Losego, M. D.; Konezny, S. J.; Fermin, D. J.; Hu, S.; Brunschwig, B. S.; et al. Characterization of Electronic Transport through Amorphous TiO_2 Produced by Atomic Layer Deposition. *J. Phys. Chem. C* **2019**, *123*, 20116−20129.
(22) Chen, X.; Liu, L.; Liu, Z.; Marcus, M. A.; Wang, W.-C.; Oyler, N. A.; Grass, M. E.; Mao, B.; Glans, P.-A.; Yu, P. Y.; et al. Properties of Disorder-Engineered Black Titanium Dioxide Nanoparticles through Hydrogenation. *Sci. Rep.* **2013**, *3*, No. 1510.
(23) Santomauro, F. G.; Lübcke, A.; Rittmann, J.; Baldini, E.; Ferrer, A.; Silatani, M.; Zimmermann, P.; Grübel, S.; Johnson, J. A.; Mariager, S. O.; et al. Femtosecond X-ray Absorption Study of Electron Localization in Photoexcited Anatase TiO_2. *Sci. Rep.* **2015**, *5*, No. 14834.
(24) Franchini, C.; Reticcioli, M.; Setvin, M.; Diebold, U. Polarons in Materials. *Nat. Rev. Mater.* **2021**, *6*, 560−586.
(25) Deskins, N. A.; Dupuis, M. Electron Transport via Polaron Hopping in Bulk TiO_2: A Density Functional Theory Characterization. *Phys. Rev. B* **2007**, *75*, No. 195212.
(26) Richter, M. H.; Cheng, W.-H.; Crumlin, E. J.; Drisdell, W. S.; Atwater, H. A.; Schmeißer, D.; Lewis, N. S.; Brunschwig, B. S. X-ray Photoelectron Spectroscopy and Resonant X-ray Spectroscopy Investigations of Interactions between Thin Metal Catalyst Films and Amorphous Titanium Dioxide Photoelectrode Protection Layers. *Chem. Mater* **2021**, *33*, 1265−1275.
(27) Wang, Z.; Wen, B.; Hao, Q.; Liu, L.-M.; Zhou, C.; Mao, X.; Lang, X.; Yin, W.-J.; Dai, D.; Selloni, A.; et al. Localized Excitation of Ti^{3+} Ions in the Photoabsorption and Photocatalytic Activity of Reduced Rutile TiO_2. *J. Am. Chem. Soc.* **2015**, *137*, 9146−9152.
(28) Liu, B.; Zhao, X.; Yu, J.; Parkin, I. P.; Fujishima, A.; Nakata, K. Intrinsic Intermediate Gap States of TiO_2 Materials and Their Roles in Charge Carrier Kinetics. *J. Photochem. Photobiol., C* **2019**, *39*, 1−57.
(29) Strand, J.; Kaviani, M.; Gao, D.; El-Sayed, A.-M.; Afanas'ev, V. V.; Shluger, A. L. Intrinsic Charge Trapping in Amorphous Oxide Films: Status and Challenges. *J. Phys.: Condens. Matter* **2018**, *30*, No. 233001.
(30) Yang, S.; Brant, A. T.; Giles, N. C.; Halliburton, L. E. Intrinsic Small Polarons in Rutile TiO_2. *Phys. Rev. B* **2013**, *87*, No. 125201.
(31) Reckers, P.; Dimamay, M.; Klett, J.; Trost, S.; Zilberberg, K.; Riedl, T.; Parkinson, B. A.; Brötz, J.; Jaegermann, W.; Mayer, T. Deep and Shallow TiO_2 Gap States on Cleaved Anatase Single Crystal (101) Surfaces, Nanocrystalline Anatase Films, and ALD Titania Ante and Post Annealing. *J. Phys. Chem. C* **2015**, *119*, 9890−9898.
(32) Qian, R.; Zong, H.; Schneider, J.; Zhou, G.; Zhao, T.; Li, Y.; Yang, J.; Bahnemann, D. W.; Pan, J. H. Charge Carrier Trapping, Recombination and Transfer during TiO_2 Photocatalysis: An Overview. *Catal. Today* **2019**, *335*, 78−90.
(33) Vequizo, J. J. M.; Nishioka, S.; Hyodo, J.; Yamazaki, Y.; Maeda, K.; Yamakata, A. Crucial Impact of Reduction on the Photocarrier Dynamics of $SrTiO_3$ Powders Studied by Transient Absorption Spectroscopy. *J. Mater. Chem. A* **2019**, *7*, 26139−26146.
(34) Yamakata, A.; Vequizo, J. J. M. Curious Behaviors of Photogenerated Electrons and Holes at the Defects on Anatase, Rutile, and Brookite TiO_2 Powders: A Review. *J. Photochem. Photobiol., C* **2019**, *40*, 234−243.
(35) Khan, R.; Ali-Löytty, H.; Saari, J.; Valden, M.; Tukiainen, A.; Lahtonen, K.; Tkachenko, N. V. Optimization of Photogenerated Charge Carrier Lifetimes in ALD Grown TiO_2 for Photonic Applications. *Nanomaterials* **2020**, *10*, No. 1567.
(36) CasaXPS: Processing Software for XPS, AES, SIMS and More. http://www.casaxps.com/ (accessed July 2, 2020).
(37) Scofield, J. H. Hartree-Slater Subshell Photoionization Cross-Sections at 1254 and 1487 eV. *J. Electron Spectrosc. Relat. Phenom.* **1976**, *8*, 129−137.
(38) Pham, H. H.; Wang, L.-W. Oxygen Vacancy and Hole Conduction in Amorphous TiO_2. *Phys. Chem. Chem. Phys.* **2015**, *17*, 541−550.
(39) Kresse, G.; Hafner, J. Ab Initio Molecular Dynamics for Liquid Metals. *Phys. Rev. B* **1993**, *47*, 558−561.
(40) Kresse, G.; Hafner, J. Ab Initio Molecular-Dynamics Simulation of the Liquid-Metal–Amorphous-Semiconductor Transition in Germanium. *Phys. Rev. B* **1994**, *49*, 14251−14269.
(41) Kresse, G.; Furthmüller, J. Efficiency of Ab-Initio Total Energy Calculations for Metals and Semiconductors Using a Plane-Wave Basis Set. *Comput. Mater. Sci.* **1996**, *6*, 15−50.
(42) Kresse, G.; Furthmüller, J. Efficient Iterative Schemes for Ab Initio Total-Energy Calculations Using a Plane-Wave Basis Set. *Phys. Rev. B* **1996**, *54*, 11169−11186.
(43) Perdew, J. P.; Burke, K.; Ernzerhof, M. Generalized Gradient Approximation Made Simple. *Phys. Rev. Lett.* **1996**, *77*, 3865−3868.
(44) Perdew, J. P.; Burke, K.; Ernzerhof, M. Generalized Gradient Approximation Made Simple [Phys. Rev. Lett. 77, 3865 (1996)]. *Phys. Rev. Lett.* **1997**, *78*, 1396.
(45) Dudarev, S. L.; Botton, G. A.; Savrasov, S. Y.; Humphreys, C. J.; Sutton, A. P. Electron-Energy-Loss Spectra and the Structural Stability of Nickel Oxide: An LSDA+U Study. *Phys. Rev. B* **1998**, *57*, 1505−1509.
(46) Morgan, B. J.; Watson, G. W. GGA+*U* Description of Lithium Intercalation into Anatase TiO_2. *Phys. Rev. B* **2010**, *82*, No. 144119.
(47) Blöchl, P. E. Projector Augmented-Wave Method. *Phys. Rev. B* **1994**, *50*, 17953−17979.
(48) Kresse, G.; Joubert, D. From Ultrasoft Pseudopotentials to the Projector Augmented-Wave Method. *Phys. Rev. B* **1999**, *59*, 1758−1775.
(49) Cromer, D. T.; Herrington, K. The Structures of Anatase and Rutile. *J. Am. Chem. Soc.* **1955**, *77*, 4708−4709.
(50) Rao, K. V. K.; Naidu, S. V. N.; Iyengar, L. Thermal Expansion of Rutile and Anatase. *J. Am. Ceram. Soc.* **1970**, *53*, 124−126.
(51) Finazzi, E.; Di Valentin, C.; Pacchioni, G.; Selloni, A. Excess Electron States in Reduced Bulk Anatase TiO_2: Comparison of Standard GGA, GGA+*U*, and Hybrid DFT Calculations. *J. Chem. Phys.* **2008**, *129*, No. 154113.
(52) Tang, W.; Sanville, E.; Henkelman, G. A Grid-Based Bader Analysis Algorithm without Lattice Bias. *J. Phys.: Condens. Matter* **2009**, *21*, No. 084204.
(53) Henkelman, G.; Arnaldsson, A.; Jónsson, H. A Fast and Robust Algorithm for Bader Decomposition of Charge Density. *Comput. Mater. Sci.* **2006**, *36*, 354−360.
(54) Yu, M.; Trinkle, D. R. Accurate and Efficient Algorithm for Bader Charge Integration. *J. Chem. Phys.* **2011**, *134*, No. 064111.
(55) Sanville, E.; Kenny, S. D.; Smith, R.; Henkelman, G. Improved Grid-Based Algorithm for Bader Charge Allocation. *J. Comput. Chem.* **2007**, *28*, 899−908.
(56) Sheet Resistance Equations and Theory|Complete Guide. https://www.ossila.com/pages/sheet-resistance-theory (accessed July 2, 2020).

https://doi.org/10.1021/acs.jpcc.1c10919
J. Phys. Chem. C 2022, 126, 4542−4554

(57) van de Krol, R.; Grätzel, M., Eds. *Photoelectrochemical Hydrogen Production*; Electronic Materials: Science & Technology; Springer US, 2012.
(58) Dufond, M. E.; Diouf, M. W.; Badie, C.; Laffon, C.; Parent, P.; Ferry, D.; Grosso, D.; Kools, J. C. S.; Elliott, S. D.; Santinacci, L. Quantifying the Extent of Ligand Incorporation and the Effect on Properties of TiO_2 Thin Films Grown by Atomic Layer Deposition Using an Alkoxide or an Alkylamide. *Chem. Mater.* **2020**, *32*, 1393−1407.
(59) Sperling, B. A.; Kimes, W. A.; Maslar, J. E. Reflection Absorption Infrared Spectroscopy during Atomic Layer Deposition of HfO_2 Films from Tetrakis(Ethylmethylamido)Hafnium and Water. *Appl. Surf. Sci.* **2010**, *256*, 5035−5041.
(60) Abendroth, B.; Moebus, T.; Rentrop, S.; Strohmeyer, R.; Vinnichenko, M.; Weling, T.; Stöcker, H.; Meyer, D. C. Atomic Layer Deposition of TiO_2 from Tetrakis(Dimethylamino)Titanium and H_2O. *Thin Solid Films* **2013**, *545*, 176−182.
(61) Rodríguez-Reyes, J. C. F.; Teplyakov, A. V. Chemistry of Diffusion Barrier Film Formation: Adsorption and Dissociation of Tetrakis(Dimethylamino)Titanium on Si(100)-2 × 1. *J. Phys. Chem. C* **2007**, *111*, 4800−4808.
(62) Driessen, J. P. A. M.; Schoonman, J.; Jensen, K. F. Infrared Spectroscopic Study of Decomposition of $Ti(N(CH_3)_2)_4$. *J. Electrochem. Soc.* **2001**, *148*, G178.
(63) Choi, W. H.; Lee, C. H.; Kim, H.; Lee, S. U.; Bang, J. H. Designing a High-Performance Nitrogen-Doped Titanium Dioxide Anode Material for Lithium-Ion Batteries by Unravelling the Nitrogen Doping Effect. *Nano Energy* **2020**, *74*, No. 104829.
(64) Braun, A.; Akurati, K. K.; Fortunato, G.; Reifler, F. A.; Ritter, A.; Harvey, A. S.; Vital, A.; Graule, T. Nitrogen Doping of TiO_2 Photocatalyst Forms a Second e_g State in the Oxygen 1s NEXAFS Pre-edge. *J. Phys. Chem. C* **2010**, *114*, 516−519.
(65) Romero-Gómez, P.; Rico, V.; Borrás, A.; Barranco, A.; Espinós, J. P.; Cotrino, J.; González-Elipe, A. R. Chemical State of Nitrogen and Visible Surface and Schottky Barrier Driven Photoactivities of n-Doped TiO_2 Thin Films. *J. Phys. Chem. C* **2009**, *113*, 13341−13351.
(66) Henkel, K.; Das, C.; Kot, M.; Schmeißer, D.; Naumann, F.; Kärkkänen, I.; Gargouri, H. In-Gap States in Titanium Dioxide and Oxynitride Atomic Layer Deposited Films. *J. Vac. Sci. Technol., A* **2016**, *35*, No. 01B135.
(67) Sherwood, P. M. A. In *Surface Analysis by Auger and X-ray Photoelectron Spectroscopy*; Briggs, D.; Grant, J. T., Eds.; IM Publications: Trowbridge, 2003; pp 531−555.
(68) Khan, R.; Ali-Löytty, H.; Tukiainen, A.; Tkachenko, N. V. Comparison of the Heat-Treatment Effect on Carrier Dynamics in TiO_2 Thin Films Deposited by Different Methods. *Phys. Chem. Chem. Phys.* **2021**, *23*, 17672−17682.
(69) Dow, J. D.; Redfield, D. Toward a Unified Theory of Urbach's Rule and Exponential Absorption Edges. *Phys. Rev. B* **1972**, *5*, 594−610.
(70) Al-Dhhan, Z. T.; Hogarth, C. A.; Riddleston, N. The Optical Absorption Edge in Thin Amorphous Oxide Films Based on Cerium Dioxide. *Phys. Status Solidi B* **1988**, *145*, 145−149.
(71) King, D. M.; Du, X.; Cavanagh, A. S.; Weimer, A. W. Quantum Confinement in Amorphous TiO_2 films Studied via Atomic Layer Deposition. *Nanotechnology* **2008**, *19*, No. 445401.
(72) Burstein, E. Anomalous Optical Absorption Limit in InSb. *Phys. Rev.* **1954**, *93*, 632−633.
(73) Panayotov, D. A.; Yates, J. T. n-Type Doping of TiO_2 with Atomic Hydrogen-Observation of the Production of Conduction Band Electrons by Infrared Spectroscopy. *Chem. Phys. Lett.* **2007**, *436*, 204−208.
(74) Asahi, R.; Morikawa, T.; Ohwaki, T.; Aoki, K.; Taga, Y. Visible-Light Photocatalysis in Nitrogen-Doped Titanium Oxides. *Science* **2001**, *293*, 269−271.
(75) Martin, N.; Rousselot, C.; Rondot, D.; Palmino, F.; Mercier, R. Microstructure Modification of Amorphous Titanium Oxide Thin Films during Annealing Treatment. *Thin Solid Films* **1997**, *300*, 113−121.
(76) Hanaor, D. A. H.; Sorrell, C. C. Review of the Anatase to Rutile Phase Transformation. *J. Mater. Sci.* **2011**, *46*, 855−874.
(77) Berera, R.; van Grondelle, R.; Kennis, J. T. M. Ultrafast Transient Absorption Spectroscopy: Principles and Application to Photosynthetic Systems. *Photosynth. Res.* **2009**, *101*, 105−118.
(78) Chen, Y. W.; Prange, J. D.; Dühnen, S.; Park, Y.; Gunji, M.; Chidsey, C. E. D.; McIntyre, P. C. Atomic Layer-Deposited Tunnel Oxide Stabilizes Silicon Photoanodes for Water Oxidation. *Nat. Mater.* **2011**, *10*, 539−544.
(79) Scheuermann, A. G.; Prange, J. D.; Gunji, M.; Chidsey, C. E. D.; McIntyre, P. C. Effects of Catalyst Material and Atomic Layer Deposited TiO_2 Oxide Thickness on the Water Oxidation Performance of Metal−Insulator−Silicon Anodes. *Energy Environ. Sci.* **2013**, *6*, 2487−2496.
(80) Scheuermann, A. G.; Lawrence, J. P.; Kemp, K. W.; Ito, T.; Walsh, A.; Chidsey, C. E. D.; Hurley, P. K.; McIntyre, P. C. Design Principles for Maximizing Photovoltage in Metal-Oxide-Protected Water-Splitting Photoanodes. *Nat. Mater.* **2016**, *15*, 99−105.
(81) Swaminathan, S.; McIntyre, P. C. Titania/Alumina Bilayer Gate Dielectrics for Ge MOS Devices: Frequency- and Temperature-Dependent Electrical Characteristics. *Electrochem. Solid-State Lett.* **2010**, *13*, G79.
(82) Scott, E. A.; Gaskins, J. T.; King, S. W.; Hopkins, P. E. Thermal Conductivity and Thermal Boundary Resistance of Atomic Layer Deposited High-k Dielectric Aluminum Oxide, Hafnium Oxide, and Titanium Oxide Thin Films on Silicon. *APL Mater.* **2018**, *6*, No. 058302.
(83) de Melo, C.; Jullien, M.; Ghanbaja, J.; Montaigne, F.; Pierson, J.-F.; Soldera, F.; Rigoni, F.; Almqvist, N.; Vomiero, A.; Mücklich, F.; et al. Local Structure and Point-Defect-Dependent Area-Selective Atomic Layer Deposition Approach for Facile Synthesis of p-Cu_2O/n-ZnO Segmented Nanojunctions. *ACS Appl. Mater. Interfaces* **2018**, *10*, 37671−37678.
(84) Liu, T.-L.; Bent, S. F. Area-Selective Atomic Layer Deposition on Chemically Similar Materials: Achieving Selectivity on Oxide/Oxide Patterns. *Chem. Mater.* **2021**, *33*, 513−523.

https://doi.org/10.1021/acs.jpcc.1c10919
J. Phys. Chem. C 2022, 126, 4542−4554